Deuteron evaporation from $N = Z$ compound nuclei

Y. Hrabar,[1,*] P. Golubev,[1] A. Idini,[1] L. G. Sarmiento,[1] B. G. Carlsson,[1] C. Müller-Gatermann,[2] W. Reviol,[2] D. Rudolph,[1] D. Seweryniak,[2] J. Wu,[2,†] H. M. Albers,[3] J. T. Anderson,[2] M. A. Bentley,[4] M. P. Carpenter,[2] C. J. Chiara,[5] P. A. Copp,[2,‡] D. M. Cox,[1] C. Fahlander,[1] U. Forsberg,[1,§] T. Huang,[2,‖] H. Jayatissa,[2,‡] T. Lauritsen,[2] S. F. D. McCaughley,[1] X. Pereira-Lopez,[4,¶] I. Ragnarsson,[1] S. Stolze,[2] S. Uthayakumaar,[4,#] and G. L. Wilson[2,6,**]

[1]*Department of Physics, Lund University, SE-22100 Lund, Sweden*

[2]*Physics Division, Argonne National Laboratory, Lemont, Illinois 60439, USA*

[3]*GSI Helmholtzzentrum für Schwerionenforschung, DE-64291 Darmstadt, Germany*

[4]*School of Physics, Engineering and Technology, University of York, Heslington, York YO10 5DD, United Kingdom*

[5]*U.S. Army Combat Capabilities Development Command Army Research Laboratory, Adelphi, Maryland 20783, USA*

[6]*Department of Physics & Astronomy, Louisiana State University, Baton Rouge, Louisiana 70803, USA*

(Received 7 February 2025; accepted 7 May 2025; published 20 June 2025)

Deuteron evaporation was observed from the $N = Z$ compound nuclei ^{52}Fe*, ^{56}Ni*, and ^{64}Ge* in an experiment conducted at Argonne National Laboratory, USA. The experiment included a novel combination of two highly pixelated double-sided Si-strip detectors inside the Microball charged-particle detection array, allowing for unequivocal discrimination of evaporated deuterons from protons and α particles. In conjunction with the Gammasphere array, Neutron Shell, and additional ancillary detectors, decay paths into various residual nuclei were investigated. The study provides insights into the competition of deuteron vs proton-neutron evaporation as a function of available excitation energy and populated angular momentum. Results are interpreted using a statistical evaporation formalism for multiple subsequent particle emissions. The decisive factor in the comparison appears to be the available excitation energy in the residual system, with single nucleon evaporation preferred over deuteron evaporation for higher excitation energies.

DOI: 10.1103/w465-w3zz

I. INTRODUCTION

Particle evaporation refers to the statistical emission of light particles, typically neutrons, protons, and α particles, from a highly excited nucleus. It happens in nuclei where the excitation energy enables particles to overcome the centrifugal and Coulomb barriers and the emission is permitted by the available Q value. Particle evaporation is an important process in both fission and fusion reactions, as it influences the resulting distribution of residual nuclei. In fission reactions, the nucleus splits into fragments with high excitation energy. These fragments often emit neutrons, protons, or other particles as they decay to less-excited states. The probability and energy distribution of particle emission is a fundamental aspect of the fission process, which can be described using statistical models [1]. In fusion reactions, collisions between atomic nuclei lead to the formation of heavier elements and the emission of particles relates to excited states in the compound nucleus. The study of particle evaporation in fusion reactions is important for understanding the dynamics of nuclear fusion and fission processes, and crucial to predict final state properties [2].

Recent work by Blank *et al.* [3] evaluated several nuclear evaporation codes commonly in use, like CASCADE [4], HIVAP [5], CNABLA [6], PACE [7], or GEMINI++ [8]. A key issue identified in that study is the need for refining fusion-evaporation cross-section calculations, as these codes tend to overestimate predicted cross sections by a substantial factor of 5–10 when compared to experimental observations approaching the proton and neutron driplines. Moreover, the study highlighted the scarcity of experimental data available for validating these models, with the existing ones often including large uncertainties. These limitations emphasize the

*Contact author: yuliia.hrabar@fysik.lu.se

†Present affiliation: Brookhaven National Laboratory, Brookhaven, USA.

‡Present affiliation: Physics Division, Los Alamos National Laboratory, Los Alamos, USA.

§Present affiliation: Cyclife Sweden AB, Nyköping, Sweden.

‖Present affiliation: Institute of Modern Physics, Chinese Academy of Sciences, Lanzhou 730000, China.

¶Present affiliation: Center for Exotic Nuclear Studies, Institute for Basic Science, Daejeon, Republic of Korea.

#Present affiliation: Facility for Rare Isotope Beams, Michigan State University, East Lansing, USA.

**Present affiliation: United Kingdom Atomic Energy Authority, Abingdon, United Kingdom.

Published by the American Physical Society under the terms of the Creative Commons Attribution 4.0 International license. Further distribution of this work must maintain attribution to the author(s) and the published article's title, journal citation, and DOI. Funded by Bibsam.

necessity for improving current models and providing more experimental data to enhance the accuracy of their predictions.

Of particular interest is the omission of deuteron evaporation in most of these codes, as they primarily focus on the emission of neutrons, protons, α particles, and subsequently photons. The exclusion of deuteron evaporation is largely because deuteron emission, which involves the release of a weakly bound neutron-proton system, has a lower probability than single nucleon emissions. Furthermore, there is a notable lack of experimental data on deuteron evaporation, both because of its presumed rarity and the technical challenges related to precise identification between evaporated deuterons and protons. The lack of experimental validation specifically for deuteron evaporation creates a substantial gap in current models. The experimental results presented in this study can be used to tailor the evaporation codes to include deuteron evaporation as part of their statistical processes.

In this paper, we present experimentally measured evaporated deuteron-γ coincidences for several compound nuclei along the $N = Z$ line, notably ^{52}Fe*, ^{56}Ni*, and ^{64}Ge*. Various dependencies on reaction channel, excitation energy, spin, and isospin can be thoroughly explored. The population of excited states from the same residue via the sequential evaporation of either a proton and a neutron or following the evaporation of a deuteron is studied for several residues, namely ^{49}Cr, ^{53}Fe, ^{61}Zn, ^{60}Cu, and ^{58}Cu. Relative production cross sections as a function of angular momentum and excitation energy are computed to assess the statistical significance of deuteron evaporation in residue formation. This study was enabled by a comprehensive experimental set-up including Gammasphere [9], the Neutron Shell [10], and numerous ancillary detectors, including a novel combination of two double-sided silicon strip detectors (DSSDs) [11] and the Microball CsI(Tl) detector array [12], facilitating reaction channel selected γ-ray spectroscopy.

The paper is organized as follows: A description of the experiment is provided in Sec. II. Theoretical considerations are outlined in Sec. III. Details of the analysis and experimental results are presented in Sec. IV. The paper concludes with a summary of the present study in Sec. V. Additional information is provided in the supplemental material [13].

II. EXPERIMENT

The experiment was conducted at the ATLAS facility at Argonne National Laboratory, USA. A ^{40}Ca^{19+} ion beam was accelerated to 106 MeV with an average intensity of about 60 enA. The target was a self-supporting ^{24}Mg foil, enriched to 99.92% and with a thickness of 0.43 mg/cm^2. The main compound nucleus was created in the fusion reaction $^{40}\mathrm{Ca} + {}^{24}\mathrm{Mg} \rightarrow {}^{64}\mathrm{Ge}^*$. The beam reacting with contaminants on the surface of the target, i.e., carbon and oxygen buildup, led to extra recoils stemming from two more compound nuclei being present in the dataset: $^{40}\mathrm{Ca} + {}^{12}\mathrm{C} \rightarrow {}^{52}\mathrm{Fe}^*$ and $^{40}\mathrm{Ca} + {}^{16}\mathrm{O} \rightarrow {}^{56}\mathrm{Ni}^*$. The nuclei of interest in this study—^{49}Cr, ^{53}Fe, ^{61}Zn, ^{60}Cu, and ^{58}Cu—were produced through various reaction channels involving either d or pn evaporation from one of the three compound nuclei. The reaction channels resulting in the nuclei considered for this study are listed in Table I. The total available energy, E_{tot}, listed for each of the residues, represents the energy available for particle evaporation and γ emission with respect to the ground state of the given residual nucleus.

TABLE I. List of compound nuclei (first column) and their reaction channels involving either d or pn evaporation (second column) with resulting residues (third column) considered in this study. The total available energy for particle evaporation and γ emission in each reaction channel is denoted as E_{tot} (last column). Note that in the case of deuteron evaporation channels, 2.2 MeV of binding energy should be added to the given E_{tot} values.

Compound nucleus	Evaporation channels	Residue	E_{tot} (MeV)
^{64}Ge*	$2pn$ or dp	^{61}Zn	23.2
	$3pn$ or $d2p$	^{60}Cu	17.9
	αpn or αd	^{58}Cu	23.3
^{56}Ni*	$2pn$ or dp	^{53}Fe	19.0
^{52}Fe*	$2pn$ or dp	^{49}Cr	11.4

The focus of the experiment was in-beam particle-γ coincidence spectroscopy based on an advanced approach for charged-particle detection. The full setup comprised two novel CD-shaped DSSDs [11] and the Microball CsI(Tl) array [12] for charged-particle detection, Gammasphere [9] and Neutron Shell [10] arrays for γ and neutron detection, respectively, with the addition of the Fragment Mass Analyzer and an Ionization chamber (IC) [14] in the focal plane for recording recoil information. This complex setup provided complementary options for selecting the desired reaction channel enabling multiparameter analysis. For the present study, only particle and γ detectors are of relevance. The 71 Ge-BGO Gammasphere detector modules, with their heavimet collimators removed, were utilized not only for γ-ray detection but also to collect information on the γ-ray multiplicity k, and sum-energy H, for assisting reaction-channel selection event by event [15].

The 32 Neutron Shell detectors replaced Gammasphere detectors at forward angles, $\theta_{\mathrm{lab}} \approx 10^\circ$–$65^\circ$, with respect to the beam direction. Note that slightly different solid-angle coverage in the center-of-mass system for the three reactions studied follows, which implies neutron detection efficiency $\varepsilon_n(^{52}\mathrm{Fe}) \gtrsim \varepsilon_n(^{56}\mathrm{Ni}) > \varepsilon_n(^{64}\mathrm{Ge})$. It is important to note that the effective neutron detection efficiencies are significantly lower than expected from neutron detector solid angle coverage. The reason was synchronization problems between the data acquisition system for the neutron detectors, on the one hand, and the data acquisition system for charged particle- and γ-ray detectors, on the other hand [16]. Standard neutron-γ pulse-shape discrimination in combination with the time-of-flight technique provided both energy and timing information for the neutrons [17]. Similarly, the pulse-shape discrimination technique was applied to distinguish between α particles and protons in the signals recorded by the Microball detectors. The ΔE-E method was used for proton, deuteron, and α-particle identification in both the combined DSSDs system and in each individual DSSD when paired with the Microball

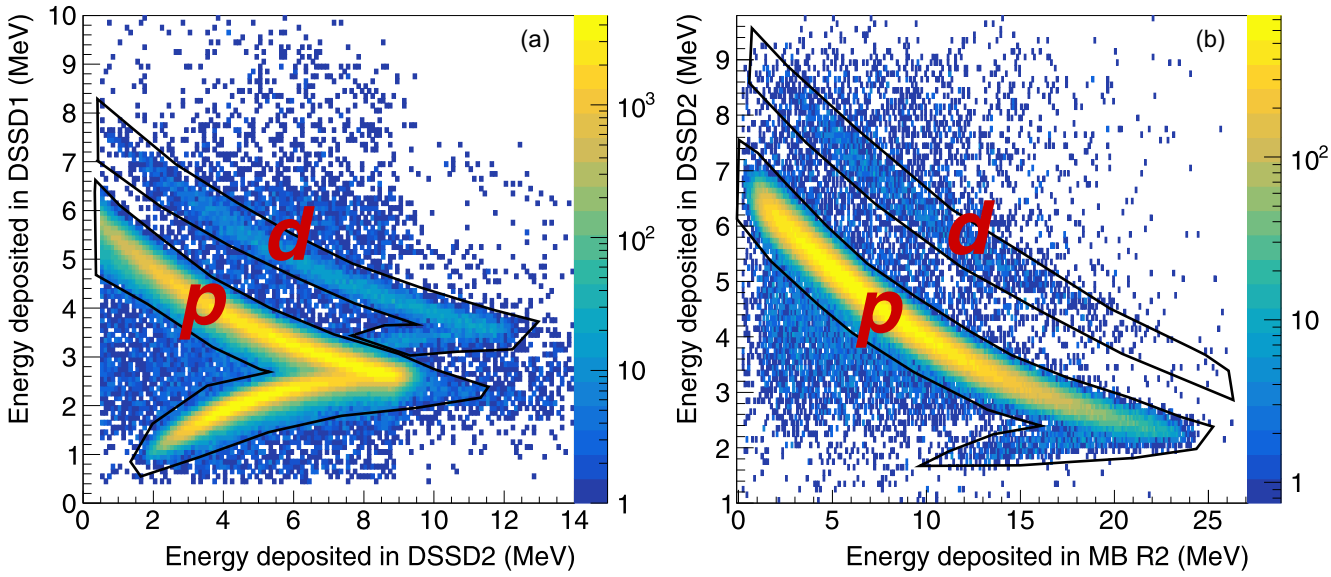


FIG. 1. Parts of ΔE-E spectra demonstrating proton-deuteron separation in the DSSD-Microball detector system. Panel (a) shows a ΔE-E spectrum for the two DSSDs, with the fourth innermost ring of DSSD 1 serving as ΔE and DSSD 2 as E detector, respectively. Panel (b) shows a ΔE-E spectrum where DSSD2 and Microball ring 2 act as ΔE and E detectors, respectively. Text labels in red denote identified proton, p, and deuteron, d, energy depositions. The color scales shown, respectively, on the right side provide the ranges of z-axis values in both panels.

rings positioned directly behind them. For more details on experimental data preparation, see Refs. [11,16].

The DSSDs allowed for unequivocal light-charged-particle identification. In addition, the high granularity of the DSSD system with 2048 pixels per detector provided excellent charged-particle tracking capabilities. This allowed for a distinct separation of proton and deuteron signals using the ΔE-E method, with angular constraints (θ and ϕ) applied to the particle trajectories. Furthermore, the discrimination between protons and deuterons was refined by conducting the ring-by-ring separation in the DSSDs, leading to a cleaner identification. Data selected for the single ring 4 of DSSD 1 are shown in Fig. 1(a). The DSSDs' ΔE-E spectrum reveals a region where proton and deuteron energies overlap. To resolve this, particles in this region were tracked further into Microball ring 2, located behind DSSD 2, and separated using the ΔE-E technique but with Microball serving as the E detector as displayed in Fig. 1(b) [11]. The particle identification patterns were confirmed through simulations of the DSSD detectors using the Geant4 Monte Carlo toolkit [18–20]. The setup's ability to unambiguously distinguish evaporated deuterons from protons, combined with Gammasphere data, serves as the foundation of the present study. It is also noteworthy that evaporated tritons were identified in the DSSDs' ΔE-E spectrum. Although the overall low number of the observed tritons prevents a quantitative analysis, their identification still represents a significant experimental observation [16].

After processing the raw experimental data, the event-by-event information available for evaporation channel selection for the current study included: detected γ rays together with measures of total γ multiplicity k, and total γ energy H, as well as the number of protons, deuterons, α particles, and neutrons detected, with their energies E, and angles θ, ϕ, and total particle energy P.

III. THEORETICAL CONSIDERATIONS

The particle evaporation process was described by Weisskopf already in 1937 with his seminal statistical model [21]. The model was later refined including the Hauser-Feshbach treatment of interference between different channels and angular momenta [22,23] and implemented in several available evaporation codes [24–27].

The probability of emitting a particle with kinetic energy E from a nucleus with excitation energy E_m^* is

$$W(E, E_m^*) = gmE\sigma \frac{\rho_d(E_d^*)}{\rho_m(E_m^*)}, \tag{1}$$

where g is the degeneracy of the final state of the emitted particle, m its mass, and σ denotes the cross section for its emission. The level density for the mother and daughter nuclei, ρ_m and ρ_d, respectively, are calculated at the corresponding excitation energies E_m^* and E_d^*. This probability of decay is given by the ratio of the phase space of the initial and final states multiplied by the cross section. The excitation energy E_d^* of the daughter nucleus can be calculated assuming that the internal excitation of the emitted particle is zero,

$$E_d^* = E_m^* - E + \mathrm{BE}_d - \mathrm{BE}_m + \mathrm{BE}_p = E_m^* - E + Q, \tag{2}$$

where BE_d, BE_m, and BE_p correspond to the binding energies of the daughter, mother, and the emitted particle, respectively, and Q the energy released in the process.

The cross section for the emission of a particle with energy E is assumed to be the geometric form factor,

$$\sigma = \begin{cases} \pi r_b^2 \left(1 - c_0 \frac{Z_d Z_p}{r_c}\right) & E \geqslant c_0 \frac{Z_d Z_p}{r_c}, \\ 0 & E < c_0 \frac{Z_d Z_p}{r_c}, \end{cases} \tag{3}$$

where r_b is a geometric radius; r_c is the Coulomb radius; Z_d and Z_p are the atomic numbers of the daughter nucleus and emitted particle, respectively; and the phenomenological factor c_0 is equal to $e^2/4\pi\epsilon_0 = 1.44\,\text{MeV fm}$. The values of these parameters are taken from the GEM2 radial parameters [28,29] which approximate quantum tunneling and other effects.

The level density of a nucleus with mass number A and excitation energy E^* is evaluated with the equidistant model from a harmonic oscillator potential,

$$\rho(E^*) = \frac{1}{\sqrt{48}} \frac{\exp(2\sqrt{aE^*})}{E^*}, \tag{4}$$

where $a = A/10$ has been chosen according to the harmonic oscillator width parametrization coming from the virial theorem [30].

The decay width Γ of a nuclear state represents the probability of emitting a particle (e.g., a neutron) from the state per unit time. Γ for a nucleus with excitation energy E^*_m, is the integral of the probability W over all possible energies of the emitted particle,

$$\Gamma = \int_0^{E^*_m + Q} W(E, E^*_m) \mathrm{d}E. \tag{5}$$

Considering subsequent emissions, the probability of a decay chain will be the product of the probabilities of each emission. In the case of one of the decay channels represented in Table I, for the first decay $E^*_m = E_{\text{tot}}$, while subsequent decay will have excitation energies of the intermediate states related by Eq. (2). The probability of the emission of two particles, 1 and 2,

$$\begin{aligned} W_{12}(E_1, E_2, E_{\text{tot}}) &= W_1(E_1, E_{\text{tot}}) W_2(E, E^*_{m2}) \\ &= g_1 m_1 \sigma_1 E_1 \frac{\rho_{d1}(E^*_{d1})}{\rho_{m1}(E_{\text{tot}})} g_2 m_2 \sigma_2 E_2 \frac{\rho_{d2}(E^*_{d2})}{\rho_{m2}(E^*_{m2})}, \end{aligned} \tag{6}$$

where subscripts $m1$ and $d1$ indicate mother and daughter of the first decay and $m2$ and $d2$ of the second. Assuming that the second emission is prompt, so that there are no intermediate γ decays and energy loss, the state of the daughter for the first decay is the mother of the second $\rho_{d1}(E^*_{d1}) = \rho_{m2}(E^*_{m2})$. This results in a dependence only on the level densities of initial compound nucleus and the final state of the decay chain,

$$W_{12}(E_1, E_2, E_{\text{tot}}) = g_1 m_1 \sigma_1 E_1 g_2 m_2 \sigma_2 E_2 \frac{\rho_d(E^*_d)}{\rho_m(E_{\text{tot}})}. \tag{7}$$

The probability of Eq. (7) can be easily generalized for the emission of n particles with energies E_i, $W(E_1, \ldots, E_n, E_{\text{tot}})$. Then the partial decay width for a sequence that ends in a given final state in the daughter nucleus,

$$\Gamma_{1\cdots n}(E^*_d, E_{\text{tot}}) = \int_{E^*_d} W(E_1, \ldots, E_n, E_{\text{tot}}) \mathrm{d}E_1 \cdots \mathrm{d}E_n, \tag{8}$$

integrating over the possible emission energies with the constraint that the energy of the final daughter nucleus in the decay chain is $E_{\text{tot}} - (E_1 + \cdots + E_n) - Q = E^*_d$.

In order to account for the beam energy loss over target penetration, we consider a Gaussian spread of the compound nucleus energy, resulting in a modified partial decay width,

$$\begin{aligned} \tilde{\Gamma}_{1\cdots n}(E^*_d) = &\int_{E^*_d} \mathrm{d}E_1 \cdots \mathrm{d}E_n \\ &\times \int_0^\infty \mathrm{d}E\, W(E_1, \ldots, E_n, E) g(E), \end{aligned} \tag{9}$$

with

$$g(E) = \frac{e^{(E_{\text{tot}} - E)^2/2b^2}}{b\sqrt{2\pi}}, \tag{10}$$

with b the width of the normalized Gaussian energy packet corresponding to the beam energy loss and E_{tot} the average compound nucleus energy in Table I. The compound ^{64}Ge is obtained through the collision of the ^{40}Ca beam with the ^{24}Mg deep inside the target, with a beam energy spread estimated at 3 MeV, reflecting a spread of the energy of the compound nucleus of $b = 0.75\,\text{MeV}$. The cases of ^{56}Ni and ^{52}Fe are obtained through contamination on or near the surface of the target ^{24}Mg, implying a small nominal beam energy spread of 0.1 MeV resulting in $b = 0.0287\,\text{MeV}$ and $b = 0.0231\,\text{MeV}$, respectively.

Considering the ratio between two different decay chains from the same compound nucleus to the same final state in the daughter nucleus, the final expression becomes independent of the level density. We define

$$R(E^*_d) \equiv \quad c\, \frac{\tilde{\Gamma}_{dp}(E^*_d) + \tilde{\Gamma}_{pd}(E^*_d)}{\tilde{\Gamma}_{ppn}(E^*_d) + \tilde{\Gamma}_{pnp}(E^*_d) + \tilde{\Gamma}_{npp}(E^*_d)}, \tag{11}$$

with c a factor that includes nuclear structure, preformation effects, and possible small systematic errors not taken into account in the corresponding experimental ratios. We have taken $c = 1/200$ to reproduce the experiment. This ratio of decay widths in Eq. (11), summed over the possible decay paths considering the corresponding cross sections can then be used for comparison with the experimentally obtained ratios $R = \frac{Y(dp)}{Y(2p)}$.

As a simple example, assuming that the cross sections for d and p emissions are the same and neglecting the beam energy spread,

$$R(E^*_d) \approx c\, \frac{g_d m_d}{g_p m_p g_n m_n \sigma_n} \frac{\int_{E^*_d} E_p E_d \mathrm{d}E_p \mathrm{d}E_d}{\int_{E^*_d} E_{p1} E_{p2} E_n \mathrm{d}E_n \mathrm{d}E_{p1} \mathrm{d}E_{p2}}. \tag{12}$$

The yield of particle emission, which is proportional to the decay width, has to be compared with the sum of experimental yields for a given excitation energy of the final nucleus. For comparison with experimental values in Sec. IV, the intensity of the γ transition from the different levels in a nucleus, in coincidence with the particle decay, is divided by the intensity

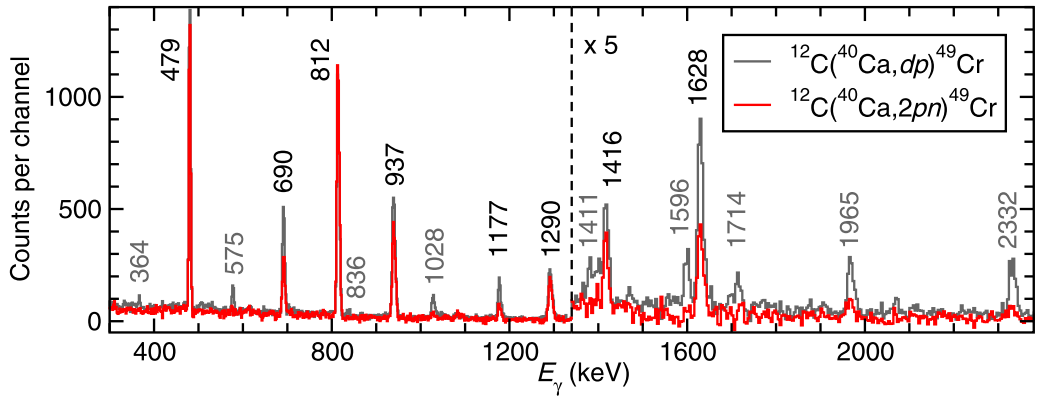


FIG. 2. Comparison of the normalized sum of γ-ray spectra in coincidence with the low-lying 272-, 479-, and 812-keV yrast transitions in ^{49}Cr produced via $2pn$ (red) or dp (dark gray) evaporation from ^{52}Fe*. The original $2pn$-selected summed spectrum was multiplied by 0.90. Energy labels are in keV. The y scale of the right-hand part of the spectra has been stretched by a factor of 5 and the binning reduced from 2 keV per channel to 4 keV per channel.

of the decay to the first excited state for normalization. This is equivalent to integrating all decays that could generate a given γ transition, i.e., all decay width above the energy E_x folded by the beam spread,

$$\sum Y_{1\cdots n}(E_x) = \frac{\int_{E_x^*}^{E_m^*+Q} \tilde{\Gamma}_{1\cdots n}(E)\mathrm{d}E}{\int_{0}^{E_m^*+Q} \tilde{\Gamma}_{1\cdots n}(E)\mathrm{d}E}. \tag{13}$$

IV. DATA ANALYSIS AND RESULTS

The selection of the reaction channel of interest was performed on an event-by-event basis by requiring the identification of the matching number of protons, deuterons, α particles, and neutrons. Once a channel is assigned to an event, a recoil vector is calculated using three parameters: (i) the presumed position within the target where the fusion-evaporation reaction occurred, (ii) the kinetic energy of the compound nucleus, and (iii) the momenta of the evaporated particles, determined from their detected energies and angles. This recoil vector was then utilized for kinematic corrections, refining the Doppler correction for γ rays, and for determination of the center-of-mass energies of the evaporated particles. Given the distinct mass differences among the studied recoils, separate sets of parameters were used for calculations corresponding to each recoil. For instance, the fusion-evaporation reaction resulting in the ^{64}Ge compound nucleus was assumed to occur at the midpoint of the target, while those reactions with contaminants forming ^{52}Fe and ^{56}Ni were assumed to occur at the target surface. This distinction changes the beam energies used to calculate the recoil excitation energies.

Following the application of refined Doppler corrections, $\gamma\gamma$ matrices were generated to analyze each recoil. Since d vs pn evaporation is studied, two matrices were produced for each nucleus of interest, corresponding to the respective reaction paths. With the additional requirement of γ coincidences associated with each channel, γ-ray energy spectra were created for each recoil. Since evaporated deuterons could only be identified using the DSSDs, to ensure a reliable comparison between the d and pn channels, the creation of the pn $\gamma\gamma$ matrix also required the detection of the proton with the DSSDs. Nevertheless, case- and reaction-dependent systematic experimental uncertainties on the level of a few percentages may persist because of slightly different effective center-of-mass angular ranges seen by evaporated protons and deuterons. Also, due to the challenges in neutron data acquisition [16], the statistics in the γ spectra significantly decreased when requiring neutron detection. To address this issue, an additional $\gamma\gamma$ matrix was created for the pn channels without requiring neutron detection. In this case, accurate channel selection relied on careful analysis of $\gamma\gamma$ coincidences.

In the following, experimental results from each of the studied cases are presented along with theoretical predictions.

A. ^{49}Cr

^{49}Cr was created from the ^{52}Fe compound nucleus through evaporation of $2pn$ or dp. Figure 2 presents γ-ray energy spectra for ^{49}Cr produced via $2pn$ or dp channels evaporation. To optimize the signal-to-noise ratio, coincidences with any of the low-lying 272-, 479-, and 812-keV yrast transitions in ^{49}Cr were required. Notably, transitions from the possibly contaminating $3pn$ (^{48}V) channel were not observed in the data. Several conclusions can be drawn from comparing these γ-ray spectra. First, both spectra exhibit sufficient statistics to support a statistically significant study. Second, the normalization factor for $2pn$ to dp was just 0.90 indicating a significant production of ^{49}Cr via dp evaporation. Finally, several γ-ray peaks, for example, those at 575, 1028, 1411, 1714, 1965, and 2332 keV, are notably more intense or only present in the spectrum of the dp channel in comparison to the spectrum following the $2pn$ evaporation. This observation suggests that specific states in ^{49}Cr were solely populated by dp evaporation calling for further investigation.

For a quantitative assessment, the ratio of yields, $R = Y(dp)/Y(2p)$, for ^{49}Cr was computed for the transitions presented in Fig. 2. The results are presented as a function of angular momentum (a) and excitation energy (b) in Fig. 3. Note that for computing the ratios in Fig. 3 only $2p$ detection was required. Comparing $2p$ data with $2pn$ data, a neutron detection efficiency of $\varepsilon_n = 11.4(6)\%$ can be derived for ^{49}Cr.

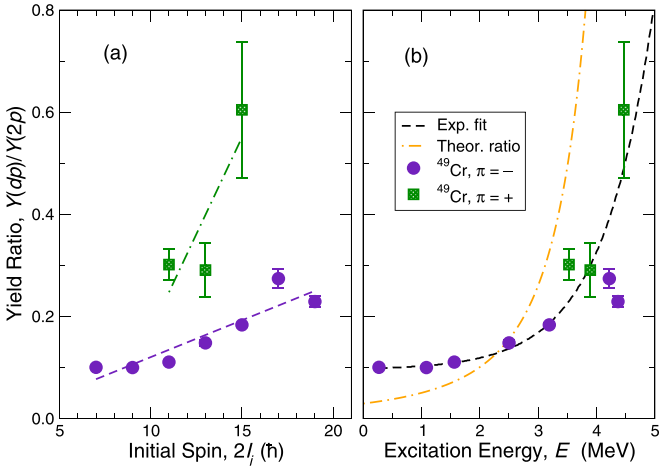


FIG. 3. Ratio of yields, $Y(dp)/Y(2p)$, for ^{49}Cr as a function of spin (a) and excitation energy (b). Ratios of positive-parity states are displayed in green and negative-parity states in purple. The lines in panel (a) are only to guide the eye. In panel (b) a least-squares fit to the observed ratios of yields as a function of excitation energy is displayed in black. The dashed-dotted orange curve shows theoretical predictions of Eq. (11). See text for details.

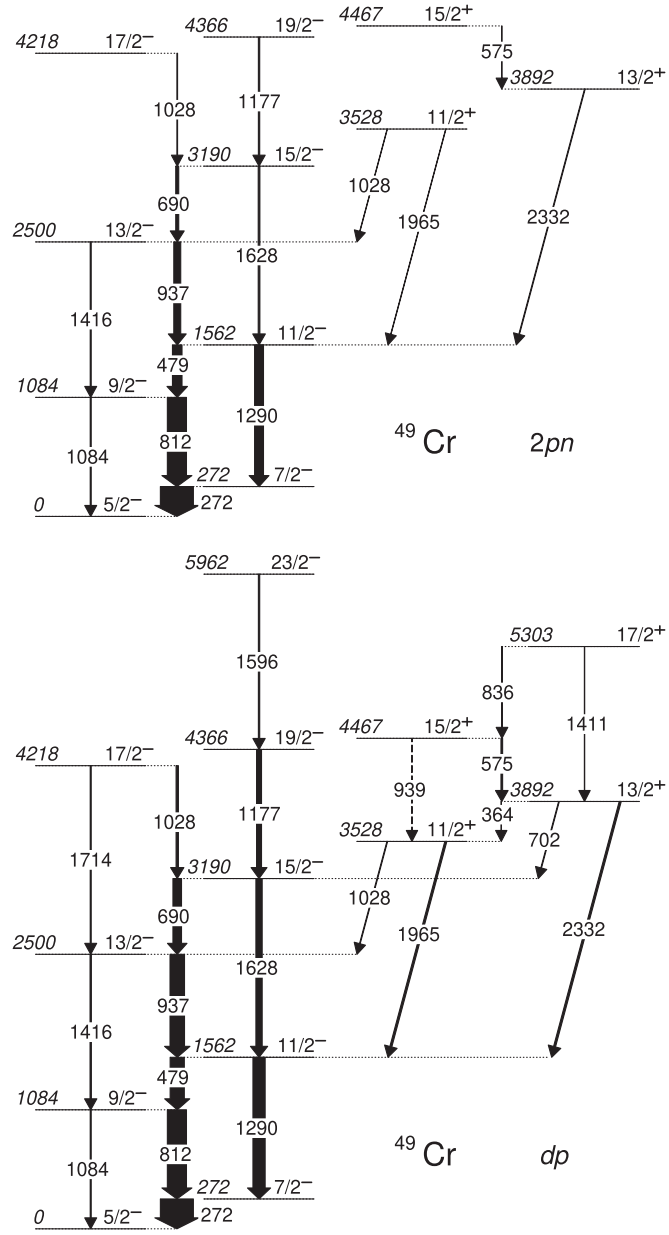


FIG. 4. Decay schemes of ^{49}Cr constructed using data from $2pn$ (top) and dp evaporation (bottom) from the compound nucleus ^{52}Fe*. The assignment of the states is done based on previous works [31–33]. Energy labels of excited states and γ-ray transitions are in keV. The widths of the arrows correspond to the relative intensity of the transitions. Tentatively placed transitions are dashed.

The assignment of the transitions was done based on the decay schemes from previous works [31–33]. The ratio of yields will tend to have an asymptote above the $E_{\rm tot}$ of the $2pn$ decay, since the $Y(2p) \to 0$ but $Y(dp)$ will be finite.

There is a clear dependency on the spin and excitation energy of the ratio which one may separate into negative- and positive-parity parts. First, for positive parity the ratio reaches $R \approx 0.6$, confirming that the relative production of ^{49}Cr via dp evaporation is significant. Second, there is an interesting feature of the experimental result of the final states in the residual ^{49}Cr nucleus, with a different ratio of yields for positive- and negative-parity states [cf. Fig. 3(a) squares and circles], though the situation is less obvious when plotting the ratios as a function of E_x [cf. Fig. 3(b)]. In the theoretical model described in Sec. III, the only factor that might be sensitive to the parity of the states is in the cross section, σ. However, to the best of our knowledge, phenomenological parametrizations of the cross section do not have a term which is both energy- and parity-dependent [1,34,35]. This might indicate a sensitivity of the experiment to the overlap between the intermediate compound ^{51}Mn wave function and the wave function of the specific state of ^{49}Cr plus deuteron, i.e., the deuteron spectroscopic factor. The spectroscopic factors of the different final states might therefore play a role in explaining the results observed, but both greater experimental statistics and dedicated theoretical investigations are required.

In the case of ^{49}Cr, the particles are emitted at energies close to the Coulomb barrier, especially for the cases with the most energy in the residual nucleus. Therefore, the results for this nucleus are quite sensitive to the parameters of the cross section describing the Coulomb barrier.

Using the peaks identified in the γ-ray spectra presented in Fig. 2, the decay schemes of ^{49}Cr produced via either $2pn$ or dp evaporation in the present experiment were constructed. Those are shown in Fig. 4. Comparing the two decay schemes shows that dp evaporation populates states of higher spin and higher excitation energy in ^{49}Cr. This implies extra excitation energy that the recoil receives through deuteron evaporation, most likely due to the additional binding energy of the deuteron.

Finally, the sums of relative yields of observed near-yrast transitions in ^{49}Cr according to the decay schemes in Fig. 4 are presented in Fig. 5 as a function of excitation energy and in steps of $\Delta E_x = 0.5$ MeV. The plot confirms the additional

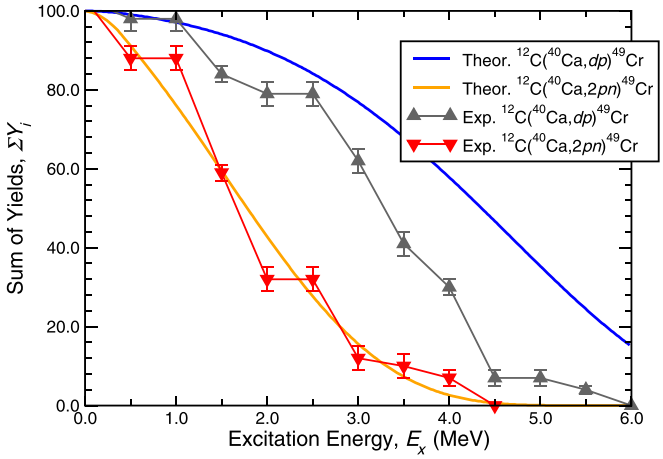


FIG. 5. Sum of relative yields of observed transitions in ^{49}Cr according to the decay schemes in Fig. 4. The sum of yields for the dp channel is displayed in gray and for the 2pn channel in red. Theoretically computed integrated yields are shown in blue for dp and in orange for 2pn evaporation calculated in Eq. (13).

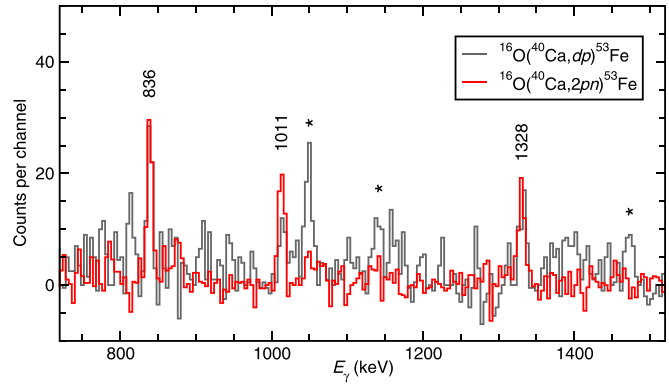


FIG. 6. Comparison of the normalized γ-ray spectra in coincidence with the 287-keV $15/2^- \rightarrow 13/2^-$ yrast transition [36,37] in ^{53}Fe produced via 2pn (red) or dp (dark gray) evaporation from the ^{56}Ni* compound nucleus. The original 2pn-selected spectrum was multiplied by 0.40. Energy labels are in keV. The stars denote transitions associated with ^{60}Cu (see Sec. IV D) because of its weak $2_2^+ \rightarrow 2_1^+$ 287-keV transition. The binning is 4 keV per channel.

binding energy available through dp evaporation. For comparison with theoretical predictions, it is important to recall that the theoretical sums of yields are computed as a function of the total excitation energy available $E_{\rm tot}$ (cf. Table I). Here the prediction of the 2pn evaporation yields zero at $E_{\rm tot} \approx 5$ MeV while dp evaporation has more energy, driven by the difference in the Q value of the final state. The Coulomb barrier for both p and d is roughly 3 MeV in this mass region, thus the comparison of experiment and theory is the most valid up to approximately this energy. The experimentally observed trend for the 2pn channel agrees very well with theoretical predictions being mostly below the barrier. The sum of yields for dp also repeats the theoretical trend and decreases as a function of excitation energy. It has a larger deviation from the theory predictions toward higher excitation energies. On the theoretical side, the statistical evaporation model in Eq. (13) integrates over all channels, including additional particle emission channels that may be open at energies larger than the Coulomb barrier. On the experimental side, only the gamma emission of a particular nucleus is considered. Furthermore, some of this deviation may also be due to the difficulties in the detection and identification of low-intensity γ-ray transitions associated with higher-lying excited states further away from the yrast line.

B. ^{53}Fe

An analysis similar to ^{49}Cr was conducted for ^{53}Fe. This nucleus was formed through 2pn or dp evaporation from the ^{56}Ni* compound nucleus as a result of the beam interacting with ^{16}O target contamination due to anticipated MgO formation on the surface of the target foil. Figure 6 displays γ-ray energy spectra produced for 2pn and dp in coincidence with the 287-keV $15/2^- \rightarrow 13/2^-$ yrast transition of ^{53}Fe [36,37]. There are only very few low-lying transitions identified for both 2pn and dp in the current dataset. Therefore, no additional figures are presented. Transitions on top of the $19/2^-$ spin-gap isomer in ^{53}Fe [36,37] were searched for but not observed in either case, possibly due to the large energy gap of more than 3 MeV above the isomer [37]. Notably, transitions from competing reaction channels are also present in the plot. Since ^{60}Cu also has a 287-keV γ-ray transition, there are several peaks visible in the spectra associated with ^{60}Cu production (cf. Sec. IV D). Other transitions from competing channels such as, e.g., ^{52}Mn, were not observed. The normalization factor used for the spectra is 0.40. The number of counts in both spectra is about 25 times lower than for ^{49}Cr.

The relative yields were computed, resulting in $Y(dp)/Y(2p) = 0.035(6)$, $Y(dp)/Y(2pn) = 0.31(5)$, which remain relatively constant across the first four transitions (287, 836, 1011, and 1328 keV) connecting the $15/2^- \rightarrow 13/2^- \rightarrow 11/2^- \rightarrow 9/2^- \rightarrow 7/2^-$ ground-state yrast cascade. This is in line with theoretical predictions for this decay. In this case, the predicted asymptote is at much higher energy with respect to the region experimentally accessible. Hence, the trend appears to be increasing at a slower pace. The neutron detection efficiency for this recoil was determined to be $\varepsilon_n = 10.7(7)\%$. The relative yields of $Y(dp)/Y(2p)$ are an order of magnitude smaller than those for ^{49}Cr signifying that deuteron emission plays a smaller role in populating ^{53}Fe residues.

C. ^{61}Zn

^{61}Zn is produced in the main ^{40}Ca + ^{24}Mg reaction following 2pn or dp evaporation. Figure 7(a) displays normalized sums of γ-ray spectra in coincidence with the 1141- and 1531-keV yrast transitions in ^{61}Zn [38,39] produced via 2pn (red) or dp (dark gray) evaporation. For instance, the 1595-keV peak assigned to the $25/2^- \rightarrow 21/2^-$ transition based on previous works [38,39] is only present in the dp spectrum. Similarly, the 1948-keV peak, corresponding to the γ transition feeding into the $15/2^+$ 4264-keV excited state in ^{61}Zn, is identified in the dp spectrum but is hardly seen in coincidence with 2pn. Note that both 1595-keV and 1948-keV transitions are tenta-

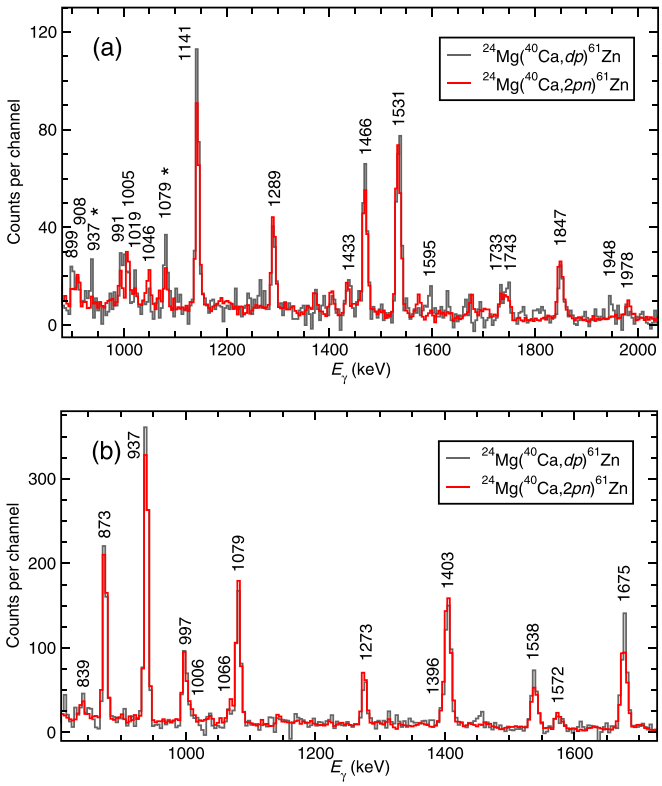


FIG. 7. (a) Comparison of the normalized sum of γ-ray spectra in coincidence with the 1141- and 1531-keV yrast transitions [38,39] in ^{61}Zn produced via $2pn$ (red) or dp (dark gray) evaporation from the ^{64}Ge* compound nucleus. (b) Same as (a) but in coincidence with the 873-, 1079-, and 1403-keV transitions. The original $2pn$-selected spectra were multiplied by 0.17. Energy labels are in keV. The stars in panel (a) denote transitions in the positive-parity yrast sequence due to coincidences with 1538-keV which overlaps with the 1532-keV transition [39] located at high excitation energies [cf. Fig. 1 in supplemental material [13] and panel (b)]. The binning is 4 keV per channel.

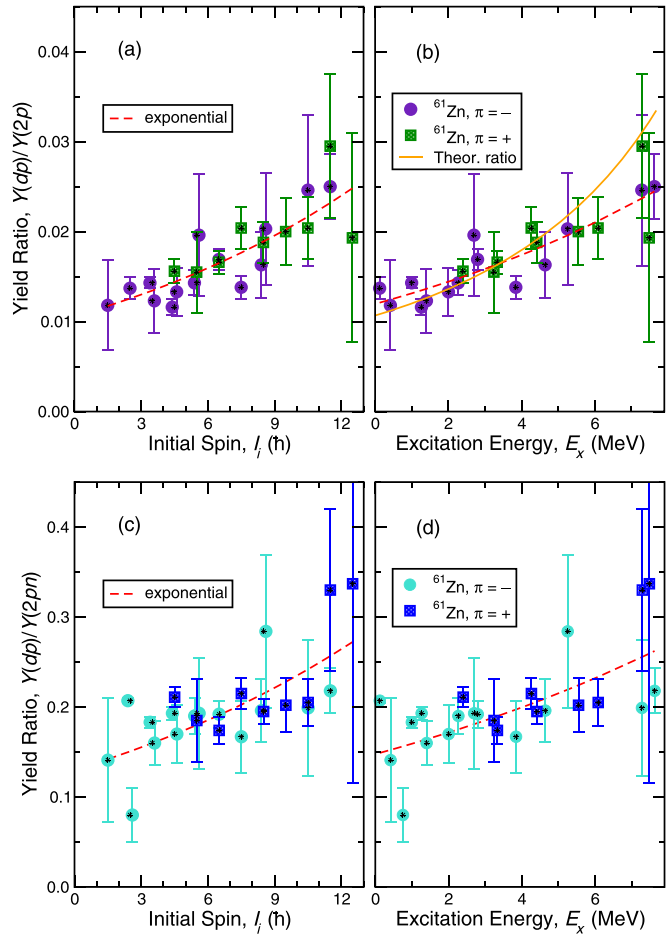


FIG. 8. Ratio of yields, $Y(dp)/Y(2p)$ [panels (a) and (b)] and $Y(dp)/Y(2pn)$ [panels (c) and (d)] for ^{61}Zn as a function of spin [panels (a) and (c)] and excitation energy [panels (b) and (d)]. Ratios of positive-parity states are displayed in green and blue, and of negative-parity states in purple and cyan, respectively. Red dashed lines in all panels represent exponential fits to the data points to guide the eye. The orange line in panel (b) corresponds to model predictions of Eq. (11). See text for details.

tively assigned due to an overall low level of statistics in the dp spectrum. However, despite much higher statistics in the $2pn$ spectrum, those transitions are difficult to see, if at all visible, in the present dataset. This implies that the corresponding excited states are weakly, if at all, populated. Figure 7(b) shows a similar energy region but instead in coincidence with the 873-, 1079-, and 1403-keV transitions. Transitions at higher excitation energy along the positive-parity yrast sequence (937, 1675, and 1538 keV [38,39]) have increasingly higher relative yield in the dp spectra compared to the $2pn$ ones.

Decay schemes built based on the observed transitions of ^{61}Zn in the present dataset for the $2pn$- and dp-evaporation reaction channels are provided in the supplemental material [13]. The ratio of yields, $Y(dp)/Y(2p)$ and $Y(dp)/Y(2pn)$, for ^{61}Zn as a function of spin and excitation energy are shown in Fig. 8. Note that neutron detection efficiency in this case is $\varepsilon_n = 7.9(13)\%$. It can be concluded that the production via dp is generally speaking relatively low. In fact, it is the lowest for all cases studied. Nevertheless, a rising trend for the yield ratios is clearly observed even in this case. Theoretical predictions for the ratio as a function of excitation energy are presented in Fig. 8(b). Also, in this case, the experimental range is at lower energies than the asymptote. However, the trend is less dramatic than in the ^{49}Cr case. The theoretical trend agrees nicely with the experimental data within the uncertainties.

Figure 9 displays the sum of relative yields of observed transitions in ^{61}Zn according to the decay schemes in Fig. 1 of the supplemental material [13] for the $2pn$ and dp channels. Note that the absolute intensities of a few transitions identified on top of the dp decay scheme are too low to extend it further according to the known one. Hence, the sum of yields cannot be extended to excitation energies beyond 8 MeV. A trend similar to ^{49}Cr is observed, where the sum of the yields decreases as a function of excitation energy. However, the important difference here is that $E_{\rm tot}(^{61}\text{Zn}) \approx 23$ MeV, which is available for particle evaporation and γ emission in ^{61}Zn, whereas $E_{\rm tot}(^{49}\text{Cr}) \approx 11$ MeV. Therefore, compared with the ^{49}Cr results, the distinction between the dp and $2pn$ curves is

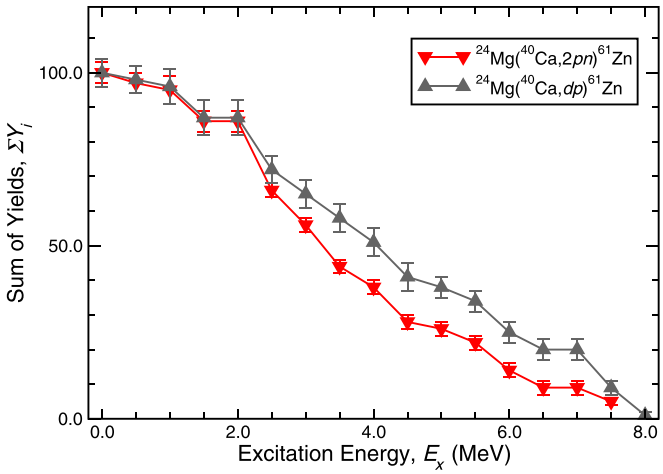


FIG. 9. Sum of relative yields of observed transitions in ^{61}Zn according to the decay schemes in Fig. 1 in the supplemental material [13]. The sum of yields for the population via the dp channel is displayed in gray and for the $2pn$ channel in red.

much less prominent. At higher excitation energies E_{tot}, more evaporation channels become energetically accessible, as the available energy exceeds the Coulomb and nuclear potential barriers for multiple particles. The $2pn$ channel, which was suppressed at lower energies, becomes feasible as the excitation energy increases. Therefore, in the case of ^{61}Zn, the $2pn$ channel can compete more effectively with the dp channel, leading to more equal γ-ray yields for both channels.

D. ^{60}Cu

^{60}Cu is produced in $3pn$ and $d2p$ reaction channels from the compound nucleus ^{64}Ge*. Comparison of the normalized sum of γ-ray spectra in coincidence with any of the low-energy transitions below the 558-keV 4^+ state in ^{60}Cu [40–42] produced via $3pn$ (red) or $d2p$ (dark gray) evaporation from the ^{64}Ge* compound nucleus is shown in Fig. 10. The original $3p$-selected spectrum was scaled by a factor of 0.13. Evidently, several peaks have higher intensity in the $d2p$ channel. Figure 10(b) displays a spectrum in coincidence with the 1046-, 1157-,1552-, and 1640-keV transitions in ^{60}Cu populated via $d2p$ evaporation. The spectrum contains many peaks not present in the $3pn$ data. In fact, a few excited states in ^{60}Cu are exclusively populated through the $d2p$ channel in the current dataset. Decay schemes of ^{60}Cu [40–42] observed as $3pn$ and $d2p$-evaporation reaction channels are shown in Fig. 2 in the supplemental material [13]. Negative-parity sequences, such as $11^- \rightarrow 9^- \rightarrow 7^-$ with 906- and 1833-keV transitions or $10^- \rightarrow 8^- \rightarrow 6^-$ with 1128- and 1365-keV transitions, are only populated via the $d2p$ reaction in the present experiment. This behavior resembles that of some of the positive-parity states in ^{49}Cr described in Sec. IV A.

Figure 11 displays the ratio of yields, $Y(d2p)/Y(3p)$, for ^{60}Cu as a function of spin and excitation energy. The neutron detection efficiency for this channel is $\varepsilon_n = 6.8(11)\%$. The conclusion that can be drawn for this case is that the $d2p$ reaction channel contributes significantly to the production of ^{60}Cu. When comparing to the other cases studied, the

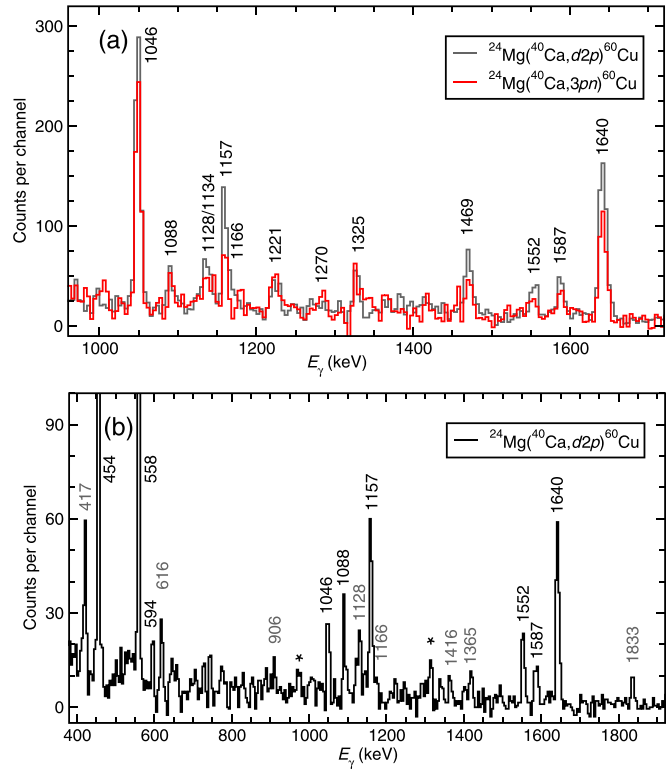


FIG. 10. (a) Comparison of the normalized sum of γ-ray spectra in coincidence with any of the low-energy transitions below the 558-keV 4^+ state in ^{60}Cu [40–42] produced via $3pn$ (red) or $d2p$ (dark gray) evaporation from the ^{64}Ge* compound nucleus. The original $3p$-selected spectrum was multiplied by 0.13. (b) Spectrum in coincidence with the 1046-, 1157-, 1552-, and 1640-keV transitions in ^{60}Cu populated via $d2p$ evaporation. Energy labels are in keV. The stars in panel (b) denote contaminating transitions from the main reaction channel ^{61}Cu [38,43]. The binning is 4 keV per channel.

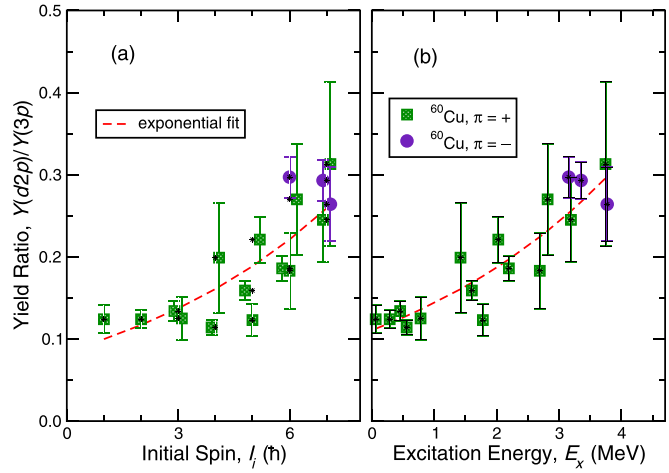


FIG. 11. Ratio of yields, $Y(d2p)/Y(3p)$, for ^{60}Cu as a function of spin (a) and excitation energy (b). Ratios of positive-parity states are depicted in green, while negative-parity states are shown in purple. Red dashed lines represent exponential fits to the data points.

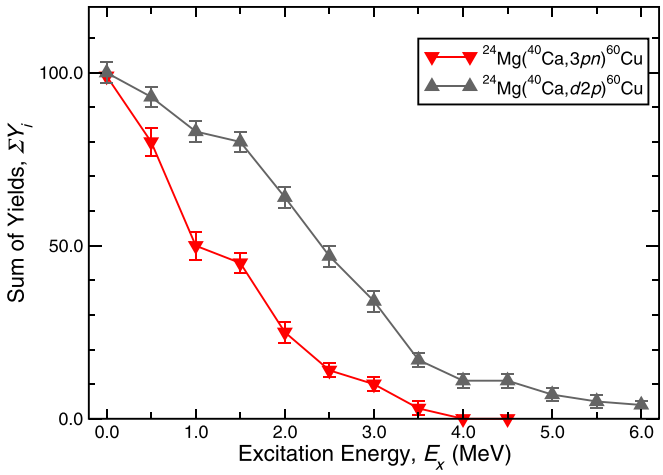


FIG. 12. Sum of relative yields of observed transitions in ^{60}Cu according to the decay schemes in Fig. 2 in the supplemental material [13]. The sum of yields for the $d2p$ reaction channel is displayed in gray and for the $3pn$ channel in red.

values of the ratios are most similar to those of ^{49}Cr, which makes deuteron evaporation the most significant for these two residues.

Figure 12 shows the sum of relative yields of observed transitions in ^{60}Cu according to the decay schemes in Fig. 2 of the supplemental material [13]. With $E_{\rm tot}$ being relatively low for this reaction channel, particles are emitted at energies close to the Coulomb barrier with little excess excitation in the residual nucleus, making this case similar to ^{49}Cr. Also in this yield curve, it is possible to clearly identify the effect of the higher Q value of the $d2p$ emission compared with $3pn$ emission.

E. ^{58}Cu

The final case for the present study is the $N = Z$ nucleus ^{58}Cu [44,45]. ^{58}Cu is observed as either αpn- or αd-evaporation channel from the compound nucleus ^{64}Ge*. Figure 13 displays a comparison of the normalized sum of γ-ray spectra in coincidence with the 444-, 515-, 1105-, and 1621-keV yrast transitions in ^{58}Cu produced via αpn (red) or αd (dark gray) evaporation. The original αpn-selected spectra were scaled by a factor of 0.45. A few small peaks from the intense $\alpha 2p$ reaction channel leading to ^{58}Ni [44,46] are also visible in the αpn spectrum.

Decay schemes of ^{58}Cu [44,45] observed as αpn- and αd-evaporation residues of the compound nucleus ^{64}Ge* are included in the supplemental material [13]. While the same transitions are observed in both cases, slight differences in intensities suggest that αd evaporation populates higher states than αpn. Figure 14 presents the ratios of yields for ^{58}Cu, namely $Y(\alpha d)/Y(\alpha p)$ in Fig. 14(a) and $Y(\alpha d)/Y(\alpha pn)$ in Fig. 14(b), as a function of excitation energy, E_x. The neutron detection efficiency for the ^{58}Cu residue is $\varepsilon_n = 7.0(13)\%$. As with other cases, the relative ratio increases with spin and excitation energy.

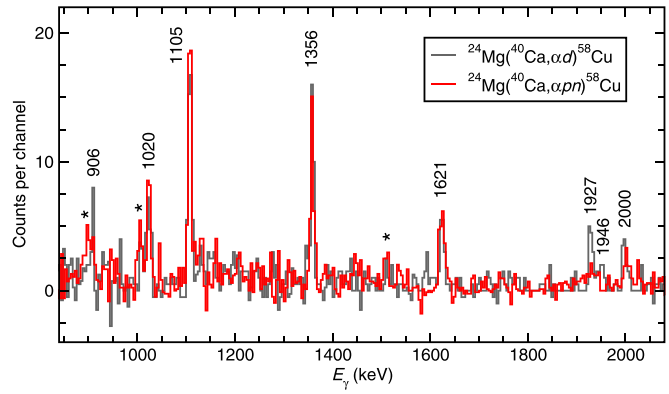


FIG. 13. Comparison of the normalized sum of γ-ray spectra in coincidence with the 444-, 515-, 1105-, and 1621-keV yrast transitions in ^{58}Cu [44,45] produced via αpn (red) or αd (dark gray) evaporation from the ^{64}Ge* compound nucleus. The original αpn-selected summed spectrum was scaled by a factor of 0.45. Energy labels are in keV. The stars denote contaminant transitions from the $\alpha 2p$ channel leading to ^{58}Ni [44,46]. The binning is 4 keV per channel.

Figure 15 presents the sum of relative yields of observed transitions in ^{58}Cu according to the decay schemes provided in the supplemental material [13]. In this case, $E_{\rm tot} \approx 23$ MeV and, thus, it is expected that the case in Fig. 15 will resemble the case of ^{61}Zn in Fig. 9; i.e., which is in line with the similarly close-lying pattern of the two yield curves. The dip in yields around 2.5–3.0 MeV relates to difficulties in observing weak decay branches from the 3420-keV 7^+ state, and in particular, the known 501-keV transition into the 5_2^+ state at 2920 keV, whether because of lack of statistics (αd and αpn matrices) or too much background at this part of the γ-ray spectrum (αp matrix).

V. SUMMARY AND OUTLOOK

In summary, individual studies of deuteron vs pn evaporation were conducted for five residual nuclei: ^{49}Cr, ^{53}Fe, ^{58}Cu, ^{60}Cu, and ^{61}Zn. The results show that the population

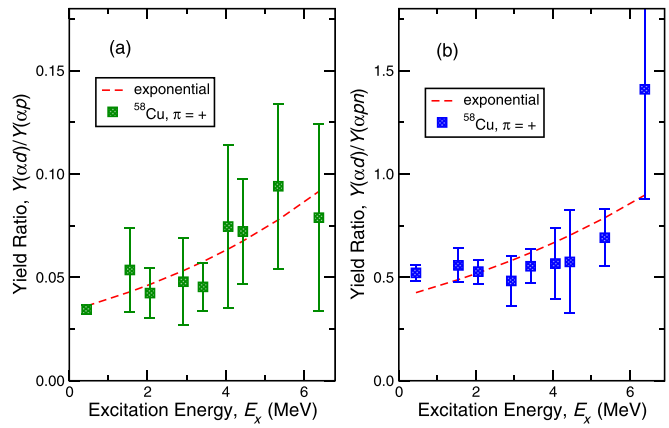


FIG. 14. Ratio of yields, $Y(\alpha d)/Y(\alpha p)$ in panel (a) and $Y(\alpha d)/Y(\alpha pn)$ in panel (b) for ^{58}Cu as a function of excitation energy, E_x. Exponential fits to data points are drawn as red dashed lines to guide the eye.

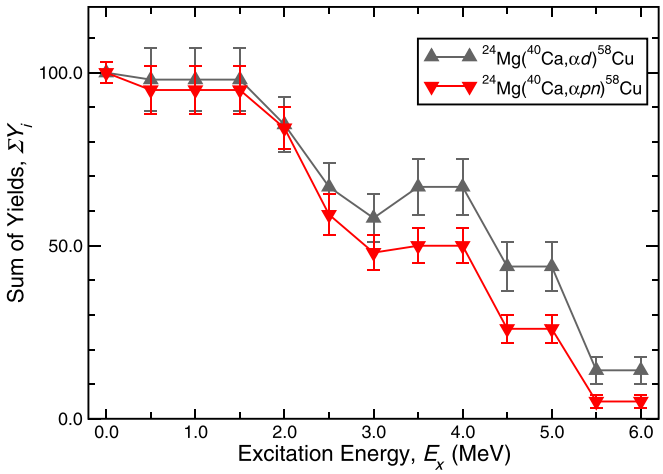


FIG. 15. Sum of relative yields of observed transitions in ^{58}Cu according to the decay schemes in Fig. 3 in the supplemental material [13]. The sum of yields for population via the αd channel is displayed in gray and for the αpn channel in red.

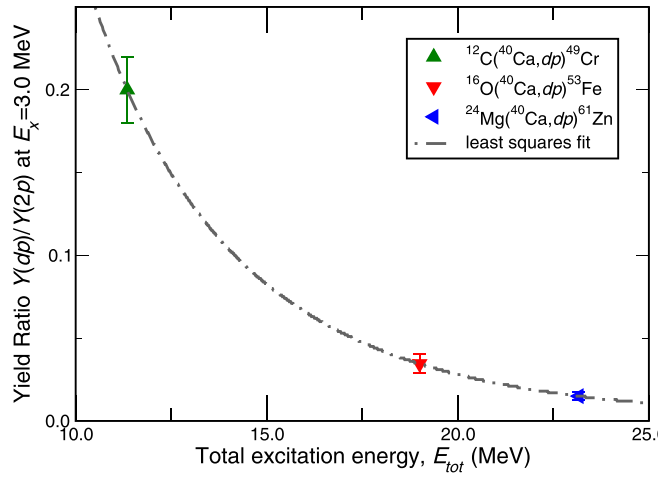


FIG. 16. Experimental ratio of yields, $Y(dp)/Y(2p)$ computed at an excitation energy $E_x = 3$ MeV for the three $2pn$ (or dp) evaporation channels ^{49}Cr, ^{53}Fe, and ^{61}Zn as a function of the total excitation energy, $E_{\rm tot}$, available for particle evaporation and γ-ray emission (cf. Table I).

of states in ^{49}Cr and ^{60}Cu exhibit significant contributions from deuteron evaporation with certain subsets of states being reached solely via deuteron evaporation. This is consistent with the extra 2.2 MeV binding energy of the deuteron being available to the system. In contrast, for ^{53}Fe, ^{58}Cu, and ^{61}Zn, deuteron evaporation plays a less significant role. As a side note, ^{58}Cu, despite being an $N = Z$ nucleus, does not show evidence of enhanced deuteron-like isospin $T = 0$ proton-neutron pairing based on this study.

A decisive factor in the studied evaporation sequences seems to be the excitation energy available in the residual system that is given by the total compound nucleus excitation energy and the Q value of the corresponding evaporation sequence. Therefore, a crucial difference between pn and d evaporation is the additional binding energy the deuteron provides to the Q value: having a compound nucleus with relatively low excitation energy, such that the charged particles have little energy to cross the Coulomb barrier, implies that the ratio $R = Y(d)/Y(pn)$ is dominated by the Q-value effect, i.e., an addition to the Q value arising from the deuteron binding energy, $\mathrm{BE}_d = 2.2$ MeV. This makes it possible to populate and observe some higher-lying states exclusively in the deuteron-evaporation sequence. In the high-statistics case of ^{49}Cr, Fig. 3 demonstrates that the asymptote of the ratio of yields is rapidly increasing towards higher excitation energies. In other cases, more energy is available for the residual nucleus, and the asymptotic behavior sets in at considerably higher excitation energy.

Since three of the studied cases, ^{49}Cr, ^{53}Fe, and ^{61}Zn, are produced through the same reaction channels, $2pn$ or dp, they can be directly compared to find a common trend. It is valuable to plot the yields of each reaction as a function of the available total excitation energy (cf. Table I), offering a systematic view of how these energies influence deuteron evaporation for the different nuclei. Figure 16 shows the ratios for each nucleus, which were extracted from their respective fits at $E_x = 3$ MeV [cf. Figs. 3(b) and 8(b) as well as Sec. IV B] and plotted as a function of the total excitation energy $E_{\rm tot}$. With higher excitation energy available for the system, single nucleon emissions become more likely, while deuteron evaporation is more prominent for lower excitation energy values. ^{58}Cu and ^{60}Cu are products of $d2p/3pn$ and $\alpha d/\alpha pn$ evaporation and thus are not included in this comparison.

Figure 16 confirms that deuteron evaporation is more likely at lower total excitation energies. This can be attributed to the Q-value effect. At low total excitation energy of the residual nucleus, the yield ratio is driven by a more probable deuteron emission due to more energy available to cross the Coulomb barrier. At higher available residual-nuclei energy, the yield ratio is driven more by the relative probability of proton and deuteron emission. This probability is influenced, in part, by the preformation factor of the deuteron.

As a final remark, to our knowledge, this is the first time in-depth γ-deuteron coincidence spectroscopy has been possible. Our theoretical model is found to reproduce extracted values and observed trends very well.

ACKNOWLEDGMENTS

We thank the ATLAS accelerator crew for their supreme efforts. This research used resources of ANL's ATLAS facility, which is a DOE Office of Science User Facility. The isotopes used in this research were supplied by the United States Department of Energy Office of Science by the Isotope Program in the Office of Nuclear Physics. This research was funded in part by the Swedish Research Council (Vetenskapsrådet, VR 2016-3969, 2020-03721, and VR 2022-3828), the Crafoord Foundation in Lund (Grant No. 20180630), the U.S. Department of Energy, Office of Science, Office of Nuclear Physics (Contract No. DE-AC02-06CH11357), and the UKRI Science and Technology Facilities Council under Grants No. ST/P003885/1 and No. ST/V001035/1.

DATA AVAILABILITY

The data that support the findings of this article are not publicly available upon publication because it is not technically feasible and/or the cost of preparing, depositing, and hosting the data would be prohibitive within the terms of this research project. The data are available from the authors upon reasonable request.

[1] D. G. Madland and A. C. Kahler, Nucl. Phys. A **957**, 289 (2017).
[2] A. Lopez-Martens, A. V. Yeremin, M. S. Tezekbayeva, Z. Asfari, P. Brionnet, O. Dorvaux, B. Gall, K. Hauschild, D. Ackermann, L. Caceres, M. L. Chelnokov, V. I. Chepigin, M. V. Gustova, A. V. Isaev, A. V. Karpov, A. A. Kuznetsova, J. Piot, O. N. Malyshev, A. G. Popeko, Yu. A. Popov *et al.*, Phys. Lett. B **795**, 271 (2019).
[3] B. Blank, G. Canchel, F. Seis, and P. Delahaye, Nucl. Instrum. Methods B **416**, 41 (2018).
[4] F. Pühlhofer, Nucl. Phys. A **280**, 267 (1977).
[5] W. Reisdorf, Z. Phys. A **300**, 227 (1981).
[6] K. Hagino, N. Rowley, and A. T. Kruppa, Comput. Phys. Commun. **123**, 143 (1999).
[7] A. Gavron, Phys. Rev. C **21**, 230 (1980).
[8] R. J. Charity, Report INDC (DNC)-530 (2008), in Joint ICTP-AIEA Advanced Workshop on Model Codes for Spallation Reactions (IAEA, Vienna, 2008).
[9] I.-Y. Lee, Nucl. Phys. A **520**, c641 (1990).
[10] D. G. Sarantites, W. Reviol, C. J. Chiara, R. J. Charity, L. G. Sobotka, M. Devlin, M. Furlotti, O. L. Pechenaya, J. Elson, P. Hausladen, S. Fischer, D. Balamuth, and R. M. Clark, Nucl. Instrum. Methods A **530**, 473 (2004).
[11] Y. Hrabar, P. Golubev, D. Rudolph, L. G. Sarmiento, C. Müller-Gatermann, W. Reviol, D. Seweryniak, J. Wu, H. M. Albers, J. T. Anderson, M. A. Bentley, M. P. Carpenter, C. J. Chiara, P. A. Copp, U. Forsberg, T. Huang, H. Jayatissa, T. Lauritsen, X. Pereira-Lopez, S. Stolze *et al.* Acta Phys. Pol. B **18**, 2 (2025).
[12] D. G. Sarantites, P.-F. Hua, M. Devlin, L. G. Sobotka, J. Elson, J. T. Hood, D. R. LaFosse, J. E. Sarantites, and M. R. Maier, Nucl. Instrum. Methods A **381**, 418 (1996).
[13] See Supplemental Material at http://link.aps.org/supplemental/10.1103/w465-w3zz for more details.
[14] C. N. Davids and J. D. Larson, Nucl. Instrum. Methods B **40-41**, 1224 (1989).
[15] C. E. Svensson, J. A. Cameron, S. Flibotte, G. Gervais, D. S. Haslip, J. M. Nieminen, J. C. Waddington, J. N. Wilson, G. C. Ball, A. Galindo-Uribarri, V. P. Janzen, D. C. Radford, D. Ward, M. Cromaz, and T. E. Drake, Nucl. Instrum. Methods A **396**, 228 (1997).
[16] Y. Hrabar, Decay modes of exotic nuclei, Ph.D. thesis, Lund University, Sweden, 2024.
[17] L. L. Andersson, A trilogy of mass A = 61: Superdeformed structures, exotic decay, and isospin symmetry, Ph.D. thesis, Lund University, Sweden, 2008.
[18] J. Allison, K. Amako, J. Apostolakis, P. Arce, M. Asai *et al.*, Nucl. Instrum. Methods A **835**, 186 (2016).
[19] J. Allison, K. Amako, J. Apostolakis, H. Araujo, P. Arce Dubois *et al.*, IEEE Trans. Nucl. Sci. **53**, 270 (2006).
[20] S. Agostinelli, J. Allison, K. Amako, J. Apostolakis, H. Araujo *et al.*, Nucl. Instrum. Methods A **506**, 250 (2003).
[21] V. Weisskopf, Phys. Rev. **52**, 295 (1937).
[22] W. Hauser and H. Feshbach, Phys. Rev. **87**, 366 (1952).
[23] P. A. Moldauer, Phys. Rev. C **11**, 426 (1975).
[24] A. S. Iljinov, M. V. Mebel, N. Bianchi, E. De Sanctis, C. Guaraldo, V. Lucherini, V. Muccifora, E. Polli, A. R. Reolon, and P. Rossi, Nucl. Phys. A **543**, 517 (1992).
[25] D. Bazin, O. Tarasov, M. Lewitowicz, and O. Sorlin, Nucl. Instrum. Methods A **482**, 307 (2002).
[26] O. B. Tarasov and D. Bazin, Nucl. Instrum. Methods B **266**, 4657 (2008).
[27] R. J. Charity, Phys. Rev. C **82**, 014610 (2010).
[28] S. Furihata, K. Niita, S.-i. Meigo, Y. Ikeda, and F. Maekawa, The GEM Code: A Simulation Program for the Evaporation and the Fission Process of an Excited Nucleus, Tech. Rep. JAERI-Data/Code 2001-015 (Japan Atomic Energy Research Inst., 2001).
[29] S. G. Mashnik, A. J. Sierk, and K. K. Gudima, arXiv:nucl-th/0208048 (2002).
[30] I. Ragnarsson and S. G. Nilsson, *Shapes and Shells in Nuclear Structure* (Cambridge University Press, Cambridge, UK, 1995).
[31] T. W. Burrows, Nucl. Data Sheets **109**, 1879 (2008).
[32] J. A. Cameron, J. L. Rodriguez, J. Jonkman, G. Hackman, S. M. Mullins, C. E. Svensson, J. C. Waddington, Lihong Yao, T. E. Drake, M. Cromaz, J. H. DeGraaf, G. Zwartz, H. R. Andrews, G. Ball, A. Galindo-Uribarri, V. P. Janzen, D. C. Radford, and D. Ward, Phys. Rev. C **58**, 808 (1998).
[33] F. Brandolini, N. H. Medina, S. M. Lenzi, D. R. Napoli, A. Poves, R. V. Ribas, J. Sanchez-Solano, C. A. Ur, D. Bucurescu, M. De Poli, R. Menegazzo, D. Bazzacco, G. de Angelis, A. Gadea, and C. Rossi-Alvarez, Phys. Rev. C **60**, 041305(R) (1999).
[34] C. Qi, F. R. Xu, R. J. Liotta, and R. Wyss, Phys. Rev. Lett. **103**, 072501 (2009).
[35] A. Soylu and C. Qi, Nucl. Phys. A **1013**, 122221 (2021).
[36] H. Junde, Nucl. Data Sheets **110**, 2689 (2009).
[37] R. du Rietz, S. J. Williams, D. Rudolph, J. Ekman, C. Fahlander, C. Andreoiu, M. Axiotis, M. A. Bentley, M. P. Carpenter, C. Chandler, R. J. Charity, R. M. Clark, M. Cromaz, A. Dewald, G. de Angelis, F. Della Vedova, P. Fallon, A. Gadea, G. Hammond, E. Ideguchi, S. M. Lenzi, A. O. Macchiavelli *et al.*, Phys. Rev. C **72**, 014307 (2005).
[38] K. Zuber and B. Singh, Nucl. Data Sheets **125**, 1 (2015).
[39] L.-L. Andersson, D. Rudolph, J. Ekman, C. Fahlander, E. K. Johansson, R. du Rietz, C. J. Gross, P. A. Hausladen, D. C. Radford, and G. Hammond, Eur. Phys. J. A **30**, 381 (2006).
[40] E. Browne and J. K. Tuli, Nucl. Data Sheets **114**, 1849 (2013).
[41] T. U. Chan, M. Agard, J. F. Bruandet, B. Chambon, A. Dauchy, D. Drain, A. Giorni, F. Glasser, and C. Morand, Phys. Rev. C **26**, 424 (1982).
[42] O. Izotova, D. Rudolph, J. Ekman, C. Fahlander, A. Algora, C. Andreoiu, R. Cardona, C. Chandler, G. de Angelis, E. Farnea, A. Gadea, J. Garcés Narro, J. Nyberg, M. Palacz, Z. Podolyák, T. Steinhardt, and O. Thelen, Phys. Rev. C **69**, 037303 (2004).
[43] L.-L. Andersson, D. Rudolph, E. K. Johansson, D. A. Torres, B. G. Carlsson, I. Ragnarsson, C. Andreoiu, C. Baktash, M. P. Carpenter, R. J. Charity, C. J. Chiara, J. Ekman, C. Fahlander,

O. L. Pechenaya, W. Reviol, R. du Rietz, D. G. Sarantites, D. Seweryniak, L. G. Sobotka, C. H. Yu *et al.*, Eur. Phys. J. A **36**, 251 (2008).

[44] C. D. Nesaraja, S. D. Geraedts, and B. Singh, Nucl. Data Sheets **111**, 897 (2010).

[45] D. Rudolph, C. Baktash, J. Dobaczewski, W. Nazarewicz, W. Satula, M. J. Brinkman, M. Devlin, H.-Q. Jin, D. R. LaFosse, L. L. Riedinger, D. G. Sarantites, and C.-H. Yu, Phys. Rev. Lett. **80**, 3018 (1998).

[46] E. K. Johansson, D. Rudolph, I. Ragnarsson, L.-L. Andersson, D. A. Torres, C. Andreoiu, C. Baktash, M. P. Carpenter, R. J. Charity, C. J. Chiara, J. Ekman, C. Fahlander, O. L. Pechenaya, W. Reviol, R. du Rietz, D. G. Sarantites, D. Seweryniak, L. G. Sobotka, C. H. Yu, and S. Zhu, Phys. Rev. C **80**, 014321 (2009).